The Astrophysical Journal, 752:130 (13pp), 2012 June 20 doi:10.1088/0004-637X/752/2/130


# THE THOMSON SURFACE. I. REALITY AND MYTH

T. A. Howard and C. E. DeForest
Southwest Research Institute, 1050 Walnut Street, Suite 300, Boulder, CO 80302, USA; howard@boulder.swri.edu
*Received 2012 February 22; accepted 2012 April 14; published 2012 June 5*

## ABSTRACT

The solar corona and heliosphere are visible via sunlight that is Thomson-scattered off free electrons and detected by coronagraphs and heliospheric imagers. It is well known that these instruments are most responsive to material at the "Thomson surface," the sphere with a diameter passing through both the observer and the Sun. It is less well known that in fact the Thomson scattering efficiency is *minimized* on the Thomson surface. Unpolarized heliospheric imagers such as *STEREO*/HI are thus approximately equally responsive to material over more than a 90° range of solar exit angles at each given position in the image plane. We call this range of angles the "Thomson plateau." We observe that heliospheric imagers are actually more sensitive to material far from the Thomson surface than close to it, at a fixed radius from the Sun. We review the theory of Thomson scattering as applied to heliospheric imaging, feature detection in the presence of background noise, geometry inference, and feature mass measurement. We show that feature detection is primarily limited by observing geometry and field of view, that the highest sensitivity for detection of density features is to objects close to the observer, that electron surface density inference is independent of geometry across the Thomson plateau, and that mass inference varies with observer distance in all geometries. We demonstrate the sensitivity results with a few examples of features detected by *STEREO*, far from the Thomson surface.

*Key words:* methods: data analysis – solar–terrestrial relations – Sun: corona – Sun: coronal mass ejections – Sun: heliosphere

*Online-only material:* color figures

## 1. INTRODUCTION

Since the discovery of coronal mass ejections (CMEs) in the 1970s (Tousey 1973), the determination of their physical properties has been dependent on the theory of Thomson scattering. CMEs are traditionally observed in visible white light by coronagraphs, most frequently on board spacecraft. These coronagraphs detect sunlight that has been Thomson-scattered off free electrons in the plasma comprising the corona and CME. Significant milestones in this theory include the works of Schuster (1879), Minnaert (1930), van de Hulst (1950), and Billings (1966). The latter reference is the most commonly cited for CME study, and is used for the analysis of white light data sets. The coronagraph, first invented by Lyot in the 1930s (Lyot 1939), has been routinely used for observations of the solar corona, and coronal transient events have been observed by ground-based coronagraphs since the 1950s (DeMastus et al. 1973). They were joined by spacecraft in the 1970s and the spacecraft coronagraph legacy includes *OSO-7* (Koomen et al. 1975), *Skylab* (MacQueen et al. 1974), *Solwind* (Michels et al. 1980), the *Solar Maximum Mission* (MacQueen et al. 1980), *SPARTAN 201* (Guhathakurta et al. 1993), the *Solar and Heliospheric Observatory*/Large Angle and Spectrometric Coronagraph Experiment (Brueckner et al. 1995), and *STEREO*/COR (Howard et al. 2008a).

In recent years, coronagraphs have been accompanied by heliospheric imagers, first by *Coriolis*/SMEI (Eyles et al. 2003) and then the *STEREO*/HIs (Eyles et al. 2009). These imagers observe unpolarized white light in the heliosphere at much larger distances from the Sun than coronagraphs, and introduce geometrical concerns independent of the optical thinness considerations that are important for coronagraphs. Vourlidas & Howard (2006) demonstrated that the Thomson scattering signal per unit electron density in the heliosphere is maximized on a locus that is quite far from the sky-plane approximation used for coronagraphs. They named this locus the "Thomson surface" (TS) and demonstrated that it is the sphere with diametric endpoints at the observer and at the Sun. They developed an analysis technique for discerning the out-of-sky-plane angle of CMEs using the sensitivity falloff, and explored important effects such as front/back asymmetry of feature brightness at a given elongation.

The TS is a compelling and useful concept that highlights the qualitative difference between interpretation of coronagraph and heliospheric data. However, its significance to image analysis and instrument sensitivity is often overstated or misunderstood. In particular, there is a widespread belief that CMEs far from the TS are not easily detectable in the heliosphere. That last inference is, in fact, a paraphrase of Vourlidas & Howard's (2006) first numbered conclusion, and it has been extensively quoted throughout the recent literature, with citations too numerous to repeat individually. This belief is plausible, both because of the calculated falloff of electron response very far from the TS along a given line of sight (LOS) and because the TS is the location where, in a heliosphere without local structure, electron density would be maximized.

However, plausibility does not imply correctness. There is a growing body of observational evidence, mostly from the *STEREO* spacecraft, that CMEs and other features are actually easily visible and seen routinely in the HI data even at quite large distances from the TS. This evidence is supported by theory, the foundation of which was published in a recent review (Howard & Tappin 2009).

In the present paper we argue that, although the TS is important to quantitative analysis of photometric heliospheric imaging data (e.g., DeForest et al. 2011), it is far less important for event detection or for gauging instrument utility than is implied by most citations to Vourlidas & Howard (2006).

We further argue that the confusion arises from the fallacy of false comparison: although objects *along a particular line of sight* (*LOS*) grow faint far from the TS, objects *at a particular distance from the Sun* grow brighter far from the TS. The latter comparison (between similar hypothetical objects at similar solar distances but different exit angles) is the correct one to make when calculating detectability of a particular type of feature by a heliospheric imager. Considering object detectability across exit angles at a given radius reveals that object detectability is limited by perspective and field-of-view (FOV) effects rather than by location relative to the TS.

Because prior discussions of coronal and heliospheric Thomson scattering (e.g., Minnaert 1930; Billings 1966; and the recent review by Howard & Tappin 2009) are more complex than needed in the heliospheric case, we summarize the elementary theory of Thomson scattering in the simple case that applies to unpolarized heliospheric imaging. We explore the breadth and flatness of an ideal instrument's response to resolved heliospheric electron density features for a variety of exit angles, and show both how it comes to be and how it differs from the same calculation on a per-electron basis. This highlights the need to consider *radiance as well as intensity* for distributed objects such as CMEs, and leads to simple formulae for the density and mass of a feature observed in interplanetary space.

In Section 2 we review scattering theory and develop the proper comparison of feature brightness and detectability for features on and off the TS. In Section 3 we discuss interplanetary transients that have been observed by heliospheric imagers far from the TS. In Section 4 we summarize the realities and myths of the TS and their importance to interpreting heliospheric images.

## 2. ELEMENTARY THEORY

Thomson scattering theory has been covered at great length by many authors, and a recent review with emphasis on heliospheric observations, including a fully general treatment of Thomson scattering, appears in Howard & Tappin (2009). Analyzing the general case of light scattered by free electrons near the Sun is quite complex as it involves an integral over the direction of sunlight coming into the scattering region. However, in the heliospheric case the Sun can be treated as small and the scattering formulae reduce to a much simpler form. For reference and clarity, we re-derive the brightness formulae here, for the small-Sun case.

### *2.1. Scattering Basics and the Thomson Plateau*

The differential scattering cross-section $d\sigma/d\omega$ may be written (e.g., Jackson 1962) as

$$\frac{d\sigma}{d\omega} = \sigma_t(1 + \cos^2\chi). \tag{1}$$

Light incident on a particular small cross-sectional area $d\sigma$ somewhere in the vicinity of an electron in interplanetary space will be scattered into a given small solid angle $d\omega$, and Equation (1) describes how that cross-section varies with the scattering geometry. The area $\sigma_t$ is half the square of the classical electron radius: $\sigma_t \equiv r_e^2/2$. Here we use $\sigma_t$ defined by Jackson (1962) and Billings (1966) as opposed to $\sigma_e = r_e^2$ used by Howard & Tappin (2009; their version of our Equation (1) included the $1/2$ term). The angle $\chi$ is just the angle of scatter: $\chi = 0$ for direct re-radiation along the line of original propagation; and $\chi = \pi/2$ for right-angle scatter. A single electron at a distance $r \gg r_\odot$ from the Sun experiences a known intensity (measured in W m$^{-2}$) of sunlight and will thus scatter a certain amount of power (measured in W) into each differential solid angle:

$$\frac{dP}{d\omega} = \sigma_t(1 + \cos^2\chi)\left\{\left(\frac{\pi r_\odot^2}{r^2}\right)B_\odot\right\}, \tag{2}$$

where $B_\odot$ is the Sun's radiance[1] (which we also call "surface brightness") of approximately $2.3 \times 10^7$ W m$^{-2}$ SR$^{-1}$, the quantity $\pi r_\odot^2 r^{-2}$ is the apparent size of the Sun (in SR) relative to the scattering site, and the quantity in curly braces is the intensity of sunlight in W m$^{-2}$ at the scattering site, also called the illumination function. However, it is not in practice possible to detect a single electron with a heliospheric imager, so instead we treat space as filled with a density of electrons per unit volume, $n_e(s, \varepsilon, \alpha)$ (we define $\alpha$ to be the azimuth around the Sun although any appropriate third coordinate would serve), and consider the power (in W) radiating from a small volume $dV = dA\, ds$ (where $s$ is a length in some direction and $A$ is an area perpendicular to it). Then Equation (2) reduces to:

$$dB \equiv \frac{dP}{d\omega dA} = \sigma_t(1 + \cos^2\chi)\left\{\left(\frac{\pi r_\odot^2}{r^2}\right)B_\odot\right\}n_e ds, \tag{3}$$

which gives the radiance $dB$ of Thomson scattering from a given small volume $dV$ located far from the observer. Choosing $s$ to be along an LOS one may now integrate to determine the surface brightness at an instrument looking at features in the heliosphere:

$$B(\varepsilon, \alpha) = B_\odot\sigma_t\pi r_\odot^2 \int r^{-2}(1 + \cos^2(\chi))n_e(s, \varepsilon, \alpha)\, ds, \tag{4}$$

where $\varepsilon$ is the elongation from the Sun of the scattering point as observed, $\alpha$ is an azimuthal angular coordinate, and $n_e$ is still the electron density function in the region being observed. The geometric values are summarized in Figure 1. Later, we find it convenient to define two separate LOS variables: $s$ and $z$, with the difference that $s$ is measured from the point of closest approach to the Sun and $z$ is measured from the observer (following Howard & Tappin 2009).

It is particularly important to work with radiance because it is the quantity (averaged over an instrument's aperture and over the solid angle subtended by a single resolution element) that is measured by a heliospheric imager. To simplify Equation (4), we can apply the Law of Sines to the triangle $(\varepsilon, \chi, \theta)$, to yield a closed-form expression for the contribution to radiance from each small packet of electrons along the LOS:

$$dB(s, \varepsilon, \alpha) = \left\{\left(B_\odot\sigma_t\pi r_\odot^2\right)(R\ \sin(\varepsilon))^{-2}\right\} \times [\sin^2(\chi)(1 + \cos^2(\chi))]n_e(s, \varepsilon, \alpha)ds, \tag{5}$$

[1] Readers are reminded that radiance (measured in W m$^{-2}$ SR$^{-1}$) is particularly useful because it is what determines the value accumulated by a focal-plane detector in a camera exposed to a distributed object. Each resolution element or pixel subtends a small solid angle $d\Omega$ and the aperture subtends a small area $d\mathcal{A}$. So long as the detected energy depends linearly on $d\mathcal{A}$ and on $d\Omega$, the power detected by a particular pixel is proportional to radiance. This relationship does not hold true for unresolved objects such as stars or individual electrons (e.g., Hecht & Zajac 1979). In image data, *average* pixel value inside a feature measures the feature's radiance, while *total* pixel value summed over the feature measures its intensity. We eschew the unmodified word "brightness" as it has been used ambiguously throughout the literature.

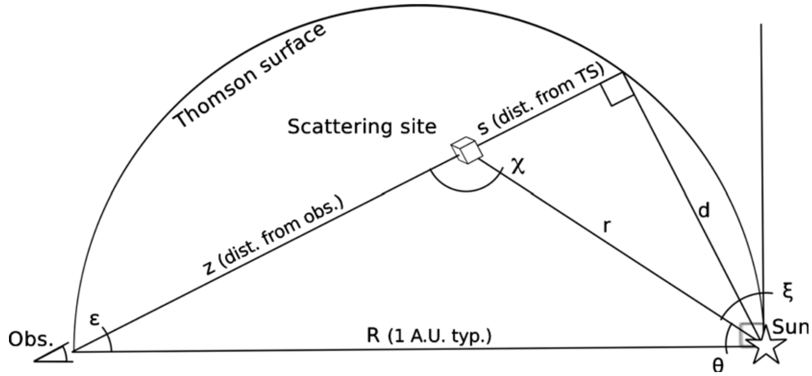


**Figure 1.** Observing diagram showing relevant angles for heliospheric imaging in the context of the Thomson scattering geometry. The line of sight with elongation $\varepsilon$ passes through the scattering site, making an angle of $\chi$ with the radial from the Sun. The distance along the line of sight is measured in terms of $s$ when measured from the Thomson surface and $z$ when from the observer.

where $R$ is the distance between the Sun and the observer. This expresses the sensitivity of an idealized heliospheric imager to electron density at various locations along its LOS. We have broken the $r^{-2}$ factor in the illumination function into an $\varepsilon$-dependent and a $\chi$-dependent component, because the former may be brought out of an LOS integral as in Equation (4), while the latter may not. Writing the terms in curly braces (which are independent of $\chi$ and therefore of $s$) as $k_{\mathrm{TS}}(\varepsilon)$ and the geometric quantity in square brackets (which depends on $s$ through $\chi$-dependence) as $G(\chi)$, the differential surface brightness becomes

$$dB = k_{\mathrm{TS}}(\varepsilon) G(\chi) n_e(s, \epsilon, \theta) ds, \tag{6}$$

where $G$ is the geometric component of the LOS integrand in Equation (4), and includes both scattering efficiency and the $\chi$-dependence of the illumination function. Vourlidas & Howard (2006) noted that this quantity is maximized on the TS (when $\chi = \pi/2$). However, the functional form of $G$ is quite flat because the $\sin^2\chi$ term (illumination) is maximized when the $1 + \cos^2\chi$ term (cross-section) is minimized. $G$ can be simplified further:

$$G = 1 - \cos^4\chi. \tag{7}$$

Simple inspection shows that the first, second, and third derivatives of $G$ with respect to $\chi$ are all zero at the TS (where $\chi = \pi/2$), so that $G(\chi)$ superosculates the function $f(\chi) = 1$ at the TS. The brightness contribution per unit length for a unit density ($dB\, ds^{-1}\, n_e^{-1}$) is thus extremely flat. The function $G(\chi)$ is plotted in Figure 2, versus $\chi$ and versus $s/d$. We henceforth refer to the region surrounding the TS where the $G$ function is flat as the "Thomson plateau," and observe that it spans roughly 90° of angle. This coincidence was first noticed over 60 years ago (van Houten 1950), and has been mentioned in passing more recently (e.g., Howard et al. 2010), but to our knowledge has never been explicitly called out for its role in simplifying interpretation of Thomson scattered images.

If ignored, $G(\chi)$ becomes a coefficient of systematic error on estimated CME mass from the photometric data, as described by Vourlidas & Howard (2006). Its flatness over a broad range of angles is the reason for the approximately constant levels of surface brightness noted by them for events at intermediate angles directed toward the Earth.

From the curves in Figure 2 it should be clear that the radiance of an object of given density observed at a particular elongation is nearly independent of its exit angle from the Sun for a broad range of angles. For example, a particular cloud of electrons observed from near Earth at 35° solar elongation will have essentially the same surface brightness whether it be 35° ahead of the limb (i.e., on the TS: $\chi = 90°$, $r = 0.57$ AU), at the solar limb (on the sky plane: $\chi = 55°$, $r = 0.70$ AU), or 70° ahead of the limb (near the observer: $\chi = 125°$, $r = 0.70$ AU).

Clarity about the difference between surface brightness (radiance) and total feature brightness (intensity) and detectability are very important because feature mass is more closely related to intensity than to radiance. Intensity is the integral of radiance over the apparent feature size, which for small features or large distances is proportional to $z^{-2}$. The integrand is just

$$dI \equiv \frac{dP}{dA} = B\, d\Omega = B\frac{dA}{z^2}, \tag{8}$$

where $\Omega$ is the apparent size of the object being viewed and $z$ is the LOS distance with origin at the observer. Of course, for small objects Equation (8) can be used directly rather than as an integrand.

Intensity is the correct value to use for calculating detectability of an object, be it resolved or unresolved. Unresolved structures, such as single electrons, are by definition smaller than the resolution element of the detecting instrument. Therefore, the instrument is unable to report the radiance of an unresolved object—only the solid angular integral of radiance, which is an intensity. Even resolved objects are distinguished against image background by a difference in signal compared with that background, and the presence or absence of a feature is most sensitively measured by integrating surface brightness over the whole feature, i.e., by detecting the feature's intensity. This relationship between feature-integrated noise and detectability holds even if the location and size of the feature are unknown, and is a fundamental aspect of digital signal processing (e.g., Vaseghi 2006).

Expanding Equation (8) to terms that are comparable to those in Equation (5),

$$dI = \left\{\frac{B_\odot \sigma_t \pi r_\odot^2}{R^4}\right\}\left[\frac{\sin^4(\chi)(1+\cos^2(\chi))}{\sin^2(\varepsilon)\,\sin^2(\varepsilon+\chi)}\right] dN_e, \tag{9}$$

where $dN_e \equiv n_e dV$ is an electron count. Equation (9) gives the differential intensity per electron in the FOV of the observer. The size of the feature is contained in $dN_e$, since $dN_e = dA\, ds\, n_e$. Figure 3 shows the difference in functional form between intensity and radiance. This difference arises because features that have larger elongation and exit angles in front of the TS

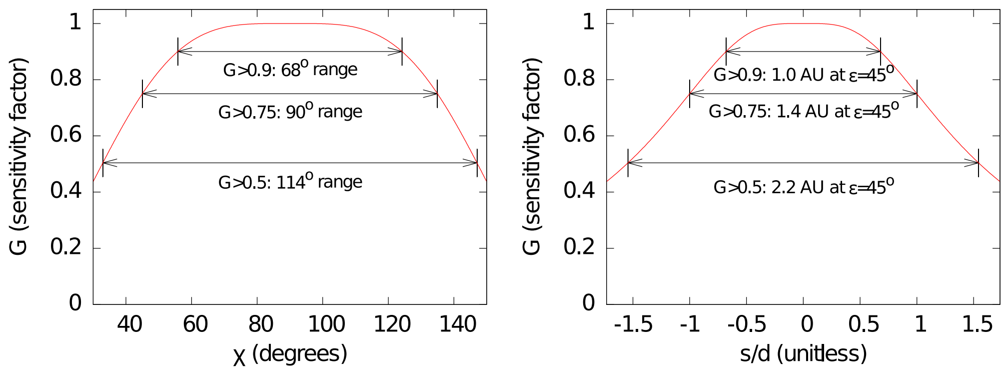


**Figure 2.** Geometric scaling factor $G$ in Equation (6) scales the differential surface brightness (radiance) per unit electron density $dB\, ds^{-1}\, n_e^{-1}$ along each line of sight from the instrument. Effects from the variation of the illumination function and from the Thomson scattering efficiency cancel, resulting in nearly equal surface brightness over a broad range of solar exit angles for a given position in the image plane. The same geometric scaling factor $G$ from Equation (6) is plotted vs. scattering angle $\chi$ (left) and the scaled distance $s/d$ from the Thomson surface (right).

(A color version of this figure is available in the online journal.)

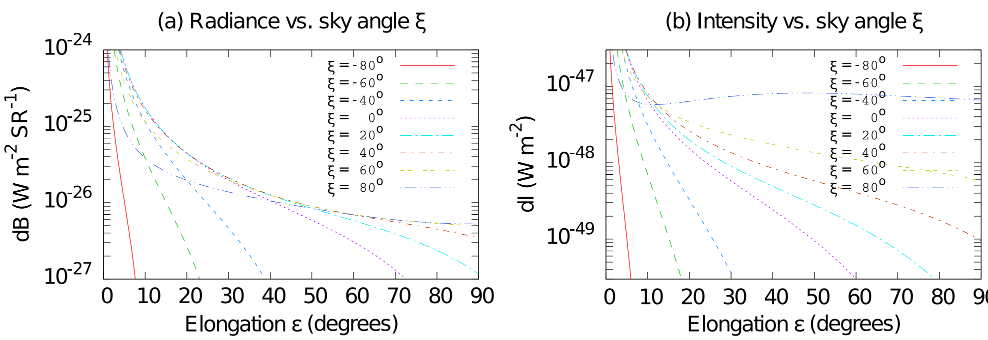


**Figure 3.** Surface brightness (radiance) and intensity vary quite differently with sky angle $\xi$. (a) Differential surface brightness associated with $dV = 1\,\mathrm{m}^3$ and $n_e = 1\,\mathrm{m}^{-3}$, vs. elongation ($\varepsilon$) for several sky angles ($\xi$) from the Sun. (b) Solid-angle-integrated differential intensity associated with the same $dV$. Integrating over the apparent size of the feature greatly enhances the detected signal at large $\varepsilon$ as the feature passes close to the instrument. See the text for discussion.

(A color version of this figure is available in the online journal.)

are close to the observer and therefore subtend a larger solid angle $d\Omega$. That proximity effect enhances the intensity of light from the feature[2] even though its radiance is independent of distance. The effect greatly enhances the total signal received from small faint features with large out-of-sky-plane angles, because perspective effects combat the decline in $G$ as the object approaches the observer. The $\xi = 80°$ curve in Figure 3(b), for example, is enhanced by multiple orders of magnitude at $\varepsilon \sim 60°$. Our Figure 3(a) is directly comparable to Figure 3 of Vourlidas & Howard (2006), and indeed the plot style for Figure 3 was chosen to correspond with that figure. Note that Vourlidas & Howard (2006) discuss "brightness" from a single electron, which is ambiguous. However, their Figure 3 is comparable in shape to our Figure 3(a) and not Figure 3(b), indicating that they have calculated a radiance (rather than an intensity). Comparing the numeric value of the curves (and including the mean solar radiance) gives a difference of some four orders of magnitude between our numeric value and theirs; we conclude that they calculated radiance of a single cm$^3$ of gas containing a density of 1 cm$^{-3}$, and subsequently verified that surmise (A. Vourlidas 2012, in preparation). Confusion between brightness and intensity is understandable, as the relevant formulae on page 150 of Billings (1966), which has been the standard reference on Thomson scattering in the corona for some four decades, include an error (described by Howard & Tappin 2009) confusing intensity and radiance; this is mostly irrelevant in the corona where the observer–object distance is nearly fixed, but becomes highly important in the heliosphere. Henceforth, for brevity, we refer to the out-of-sky-plane angle $\xi$ as simply the sky angle.

The difference between the total feature intensity and feature surface brightness across object location along a particular LOS is particularly intriguing because it changes the locus of maximum measurement sensitivity. It is no coincidence that the various lines in Figure 3(a) are in close proximity where $\theta + \varepsilon \sim 90°$: that is a geometric representation of the flatness of the $G$ function plotted in Figure 2, on and around the TS. However, the lines in Figure 3(b) show a quite different pattern, indicating that the locus of maximum *intensity* (total integrated feature brightness) is quite different from the TS. That result is particularly important, because the detectability of a feature is more closely related to its intensity than to its surface brightness, as is discussed in Section 2.3 below.

### 2.2. Feature Radiance across Sky Angle

Comparing feature surface brightness against sky angle $\xi$ and elongation $\varepsilon$ is appropriate for determining mass correction factors for a feature observed at a known elongation angle, but not appropriate for determining how well an instrument can detect features at different exit angles. The reason is that at a given $\varepsilon$, the feature illumination function, which describes the intensity of sunlight at the object location, varies with $\xi$. Figure 2 shows the effect of holding $\varepsilon$ fixed and adjusting $r$ to allow $\chi$ or, equivalently, $s/d$ to vary. Along a particular LOS,

[2] Following common practice, we use "feature" to mean either an identifiable object in 3D space or its associated image at an instrument focal plane. Where the meaning is not clear we use "object" to highlight a physical body in 3D space.

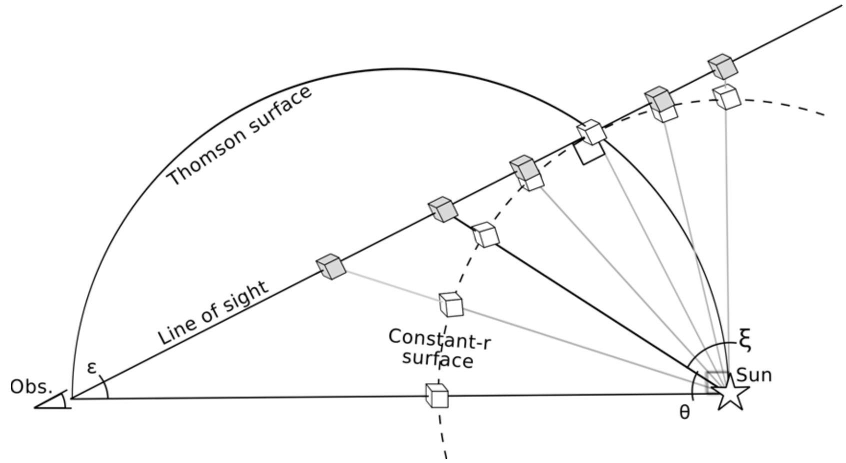


**Figure 4.** Constant-$\varepsilon$ comparisons of surface brightness are useful for interpreting data, but constant-$r$ comparisons are important to determine how well an instrument will detect CMEs at various exit angles. Small volumes (cubes) are shown at various locations relative to the different circumstances. Gray cubes indicate a volume along the line of sight (constant $\varepsilon$), while the white cubes represent the same volume along the constant-$r$ surface. The sky angle $\xi$ and its complement $\theta$ are indicated.

features far from the TS are also farther from the Sun (i.e., have larger $r$) than features close to the TS.

To determine whether an instrument can detect a feature far from the TS, one must examine how feature surface brightness and intensity vary with sky angle $\xi$ or its complement, the exit angle $\theta$, at a given distance $r$ from the Sun rather than at a fixed $\varepsilon$. The situation is diagrammed in Figure 4: The filled/gray cubes represent hypothetical identical structures at different exit angles along the LOS, while the clear cubes represent the same structures at different exit angles at the same radius from the Sun. Comparing across the latter is better for measuring detectability since (1) essentially all heliospheric features pass through all of the radial distances as they are swept out by the solar wind and (2) comparing at constant $r$ preserves the illumination function, eliminating bias from the comparison between different hypothetical features leaving the Sun at different angles.

The illumination bias imposed by considering features at a single $\varepsilon$ has historically been ignored, which is appropriate for coronagraphic or near-Sun heliospheric imaging, where the radial gradient of background intensity is high. In that case, lines of sight close to the Sun impose high background noise, so that features with large $\xi$ (and therefore small $\varepsilon$ for a given value of $r$) have a far higher noise background, and detectability suffers. But far from the Sun where the image background (and therefore noise level) is dominated by the starfield, the background noise level is approximately independent of $\varepsilon$, and feature detectability is primarily driven by signal strength rather than by a strong radial gradient in background noise. Feature detectability is discussed at greater length in Section 2.3 below.

Holding $r$ constant and allowing $\varepsilon$ to vary with $\xi$ changes the qualitative picture presented in Figures 2 and 3. Figure 5 shows the difference between the two types of calculations. The left-hand column shows radiance and intensity for the same feature as Figure 3, at each of several constant values of $\varepsilon$. This is from the same calculation as presented in Figure 3, but plotted versus the sky angle $\xi$ for constant $\varepsilon$ to highlight the comparison across solar exit angles. The shape of the plotted radiance curve follows the functional form of $G$ in Equation (7) and Figure 2. We have marked the intersection with the TS with a vertical bar across each curve. From the location of those bars it is evident that the radiance versus $\xi$ curve is, as expected, symmetric about the TS. (This symmetry is broken by the $z^{-2}$ dependence in the intensity plots at bottom, and by the asymmetry in the geometric $\varepsilon(\xi)$ relation in the radiance versus $\xi$ plot at constant $r$ at top right.)

The upper right plot in Figure 5 shows how radiance varies with solar exit angle at fixed values of $r$ that are chosen to match the $\varepsilon$ values at left on the TS. Note that the value of the plot is the same between left and right at the (marked) TS because the constant-$r$ loci are tangent to the corresponding constant-$\varepsilon$ loci there. With $r$ held constant, the illumination term in Equation (6) cannot counteract the local minimum in scattering efficiency near the TS: The TS is a *minimum* in feature radiance because of the $(1 + \cos^2 \chi)$ dependence of the Thomson cross-section. This is important because each solar wind feature passes through all observable values of $r$ in the course of its departure from the Sun. *Considering the spatial extent of a solar wind feature, the TS thus represents the exit angle with minimum radiance at a given distance from the Sun.*

The concept of TS as local radiance maximum against LOS position of a hypothetical object is important for comparing the relative brightness of many features that are superposed at the same image plane location. If the density function along the LOS contains many small local maxima ("objects") with approximately the same line integrated density ("surface density") in each object, then the objects closest to the TS will appear brightest in the superposed stack of corresponding features in the image plane. If the radiance maximum were particularly narrow or sharp, the objects closest to the TS would generally dominate the image. But we have already demonstrated that the Thomson plateau in Equation (6) is quite broad (varying by less than a factor of two over a range of nearly 120° in $\xi$) so that similarly dense, similarly sized objects over a broad range in $\xi$ must have similar surface brightness in unpolarized heliospheric image data. Therefore the observed features are not dominated by the few objects that happen to be closest to the TS. Furthermore, in the most common application of wide-field heliospheric imaging (viewing CMEs), it is unlikely that another significant structure lies on the same LOS as the CME, so it is unlikely to be confused with other fainter solar wind objects closer to the TS, regardless of its exit angle.

Similarly, because of the flatness of the Thomson plateau, the surface brightness of features in the focal plane depends entirely on the surface density of each object and its elongation $\varepsilon$, for a wide range of distances from the TS.

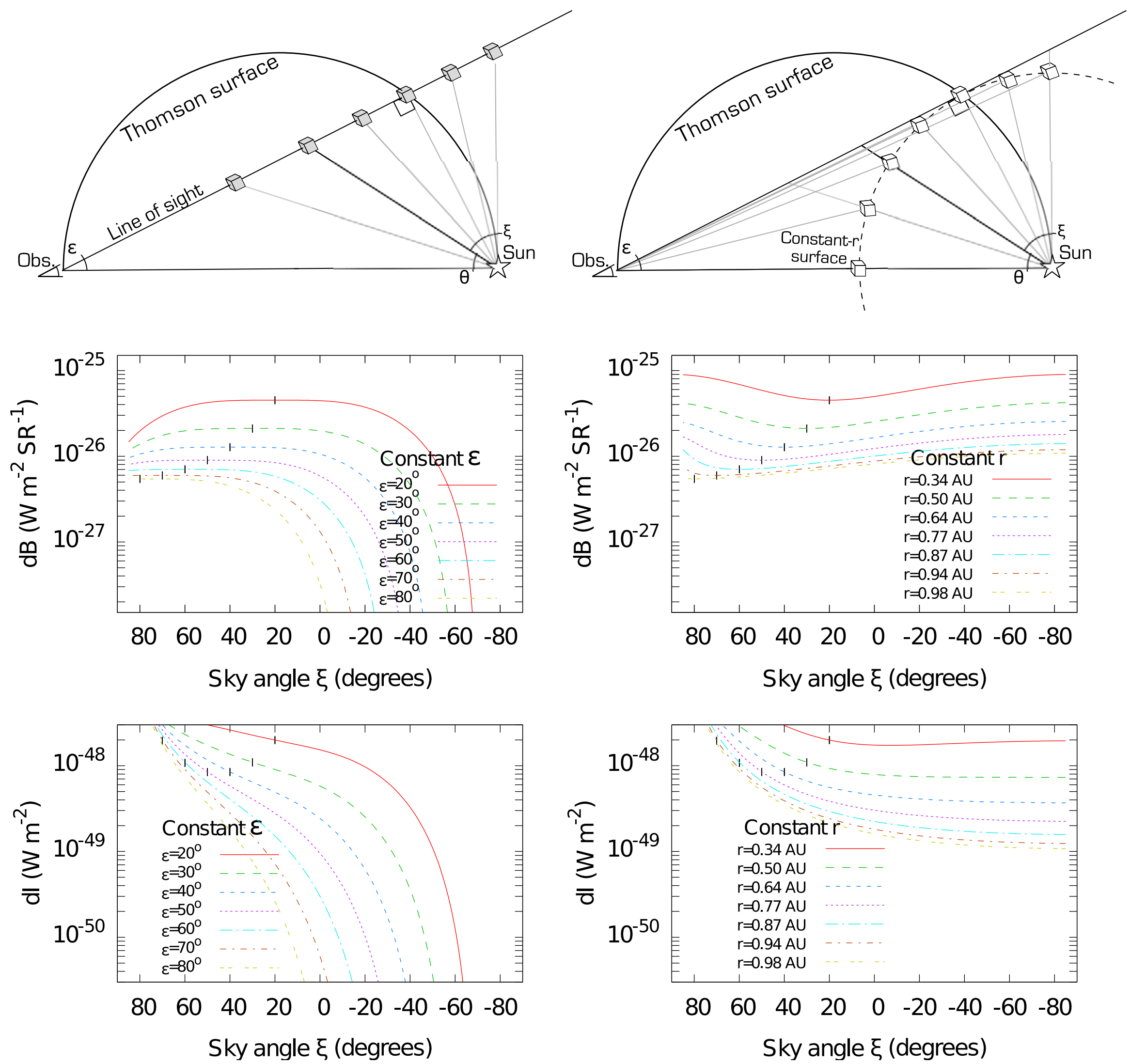


**Figure 5.** Comparing the same hypothetical cube of plasma at constant $r$ (rather than constant $\varepsilon$) eliminates illumination effects. Left: surface brightness $dB$ and intensity $dI$ at constant $\varepsilon$ are important for understanding how to interpret individual images, and are plotted vs. $\xi$ for different lines of sight (defined by their elongation $\varepsilon$). Right: $dB$ and $dI$ at constant $r$ show how well an instrument will detect CMEs at a given exit angle. In all plots, the intersection of each line with the TS is noted. The TS marks a (very weak) maximum in radiance from the unit volume *only* in the constant-$\varepsilon$ comparison (upper left). In the constant-$r$ comparison, the TS marks a *minimum* in radiance (upper right). The TS is not particularly important to the intensity of small features, either in the constant-$\varepsilon$ or the constant-$r$ comparisons (lower two plots), because the proximity effect of feature apparent size overwhelms the illumination and Thomson scattering effects on radiance.

(A color version of this figure is available in the online journal.)

The plots at the bottom of Figure 5 show variation in the observed intensity of a single electron with $\xi$. The proximity (apparent size) effect in the intensity overwhelms the Thomson scattering effects, so that there is no ideal distance at which intensity is maximized for sufficiently small features. For features that are not small compared to $z$, the plotted rise in intensity with shrinking $z$ rolls over when $z \sim l$, the length scale of the object in three-dimensional (3D) space. At shorter distances the feature's subtended solid angle is no longer proportional to $z^{-2}$ as assumed in Equation (8), but this distance and peak intensity depend on the size of the object rather than on the geometry of the Thomson plateau or any other peculiar aspect of Thomson scattering.

### 2.3. *Feature Detectability across Sky Angle*

Detectability of a particular feature is determined by its level above a noise floor. We have found (DeForest et al. 2011) that the background "image floor" far from the Sun is nearly constant (neglecting Galactic effects) in heliospheric images from *STEREO* away from the center of the zodiacal light band that marks the plane of the ecliptic. For example, over most of the *STEREO*/HI-2 FOV, the noise floor is determined primarily by photon and image structural noise from the background starfield (DeForest et al. 2011), which are nearly uniform random variables that are independently sampled in each resolution element of the image. Hence, if a heliospheric feature has apparent size $\Omega$, then its total intensity at the camera is approximately $I = B_{\mathrm{av}}\Omega$ (where $B_{\mathrm{av}}$ is the feature-averaged radiance which is measured as average pixel value). Assuming that the background noise is a random variable with approximately uniform characteristics and a constant number of samples per unit solid angle, the noise against which the feature is to be detected scales as $N = L\Omega^{0.5}$, where $L$ depends on the instrument and background subtraction method. The signal-to-noise ratio (S/N) of

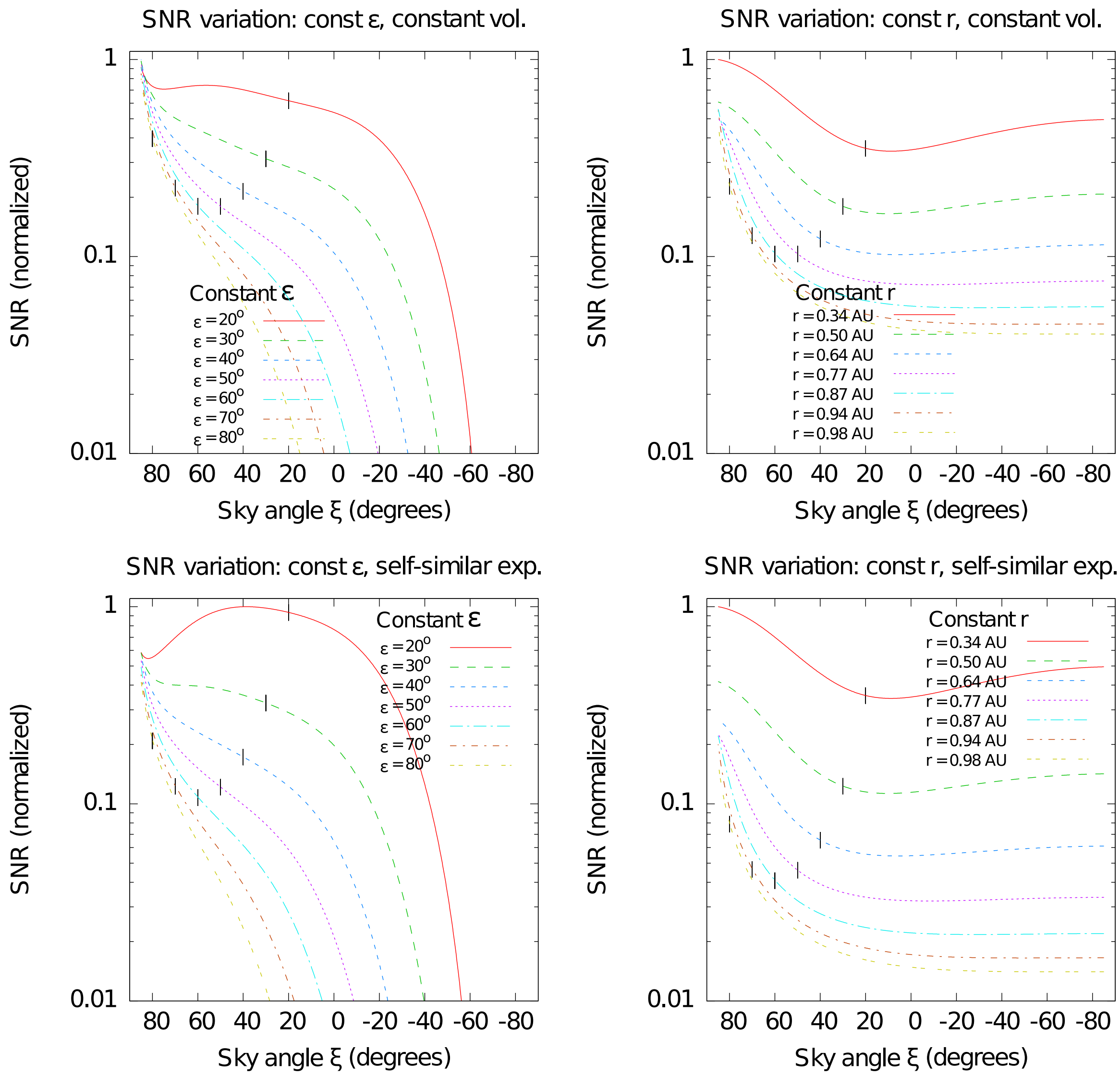


**Figure 6.** Variation of S/N for hypothetical features with a constant-brightness (stellar) background, under various conditions. As with Figure 5, the left column shows variation along the line of sight, holding $\varepsilon$ constant, while the right column shows variation around a sphere centered on the Sun, holding $r$ (and therefore the illumination) constant. The top two plots show S/N variation for a hypothetical differential volume with unit $n_e$, as considered above; and the bottom two plots show S/N variation for a hypothetical self-similarly expanding volume (as in some CMEs) with little or no accretion (which is pessimistic compared with actual CME behavior). See the text for discussion.

(A color version of this figure is available in the online journal.)

a given detection thus scales as

$$S/N = IN^{-1} = BL^{-1}\Omega^{0.5}. \tag{10}$$

This behavior is quite different from the behavior of coronagraphs, for which there is a strong $\varepsilon$-dependent noise term because coronal images have very sharp radial gradients in intensity and therefore in noise level (e.g., Brueckner et al. 1995, and references therein) that are simply not present in far-field heliospheric images.

Figure 6 shows variation of the S/N with sky angle $\xi$, normalized to the maximum value in each plot (though S/N is comparable across lines within each plot). The two cases were chosen to bracket the real behavior of solar wind objects. The top curves show the S/N behavior for a hypothetical bolus of plasma that propagates outward with constant volume, while the lower curves show the S/N behavior for a hypothetical bolus of plasma that expands self-similarly as it travels away from the Sun, i.e., whose presented $dA$ varies in proportion to $r^2$ rather than remaining constant. This does not affect the total intensity of the feature (compared to remaining compact) but does affect its apparent size (subtended solid angle $\Omega$), and therefore the noise term.

It is again important to stress the difference between the left and right columns in Figure 6. The left (constant-$\varepsilon$) plots describe S/N variation across different features *seen along the same LOS,* which is useful for interpreting a feature seen at a particular location in the focal plane of an instrument. The right (constant-$r$) plots describe S/N variation across different features *taken from the whole population of features exiting the Sun*, which is useful for understanding how a particular instrument samples that population. Because actual S/N depends on the instrument, feature density, and other incidentals, we present only a normalized geometric factor on the S/N, showing how S/N varies with $\omega$. While the S/N does

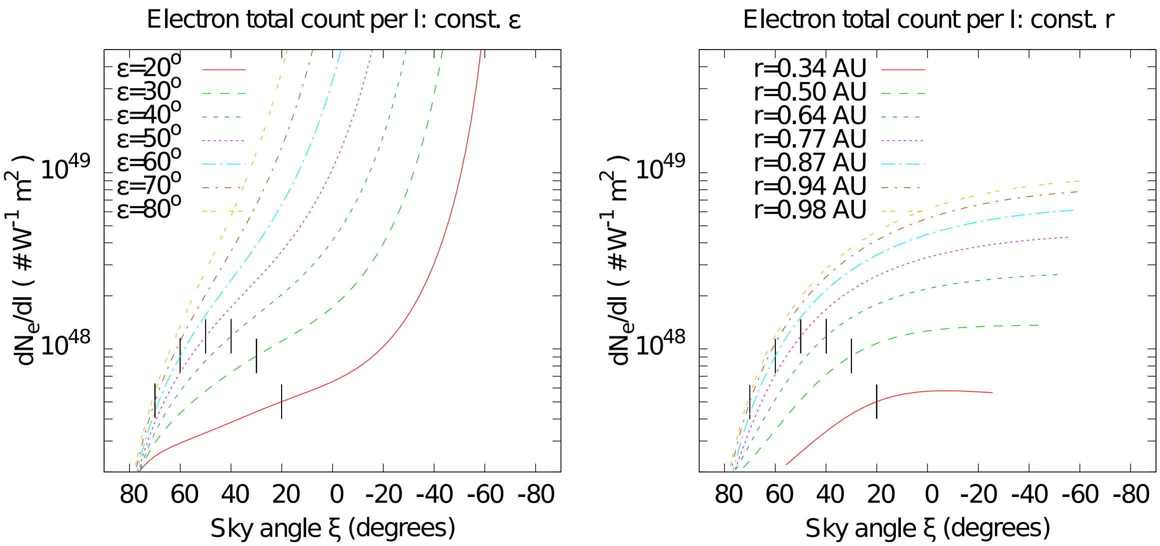


**Figure 7.** Plots of the mass calculation coefficient $dN_e/dI$ from Equation (11), for comparison along the line of sight (left) and at constant distance from the Sun (right). The TS location is marked as a vertical black bar on each trace. The distances at right are chosen to match the TS distance from the Sun for the elongation angle of each trace at left. Distance effects (both from the Sun and the observer) dominate the curve shape.

(A color version of this figure is available in the online journal.)

vary with $\xi$, it does not do so by a large factor. Features with $r = 0.64$ AU (which have a maximum elongation of $\varepsilon = 40°$ when $\xi = 40°$) are in the FOV of *STEREO*/HI-2, for example, at sky angles $\xi$ between $+75°$ and $-35°$ (both of which set $\varepsilon \sim 20°$). Over that range, S/N varies by only a factor of three (from a scaling factor of 0.3–0.1 in the plot at upper right of Figure 6). It is important to note that, although we have ignored zodiacal light in the S/N calculation, the zodiacal light does not affect the comparison of S/N ratio between the two extrema of $\xi$ observable at a single $r$ and $\varepsilon$, since the extrema occur at the same location in the image plane and are therefore measurable against the same background.

While S/N variation by a factor of 3–10 does affect detectability of some types of object, CMEs are particularly bright and large. Using *STEREO*/HI-2, DeForest et al. (2011) and Howard & DeForest (2012) found typical S/N of 10 in bright features in each 1°.5 square patch of sky. They observed several CMEs subtending hundreds of square degrees, for a detection S/N (integrated over each whole CME) of the order of several hundred. Based on the plots on the right-hand column of Figure 6, which show detection S/N versus $\xi$ and include the $z$-dependent perspective effects, we conclude that comparable CMEs would be detectable with S/N > 10 at all geometrically allowed values of $\xi$ (i.e., inside the FOV) with that instrument. Hence, *radiance- and TS-related effects do not drive detection of CMEs in contemporary heliospheric imagers.*

Let us now turn to a brief discussion of the features in Figure 6. The left-hand column is dominated by perspective effects and the familiar $z^{-2}$ dependence of feature intensity due to the variation of the feature's apparent size with observer–feature distance $z$. (Incidentally, dropping this $z^2$ term is the error made by Billings (1966) and described by Howard & Tappin (2009).) Because, in this picture, noise scales with $z^{-1}$, the S/N scales as only $z^{-1}$ rather than $z^{-2}$, even in the absence of any variation in the $G$ term of Equations (6) and (7). The upper left panel of Figure 6 shows particularly well the interplay between the variation of $G$ and $z^{-1}$, reflecting the plateau structure of $G$ (plotted in Figure 2) and the tilt due to variation of $z$ with the solar sky angle $\xi$.

### *2.4. Feature Mass across Sky Angle*

To find the mass of an observed feature, one must invert Equation (4) to solve for the total number of electrons $N_e$ in the feature. For large features the integral is nontrivial and must be treated with many simplifying assumptions. For a surprisingly large array of features, however, the integrand may be treated as constant and the integral reduces to a simple multiplication—whereupon Equations (6) and (8) may be used directly (DeForest et al. 2011). Solving the desired Equation (6) for $dN_e$ yields the small-feature formula:

$$dN_e = \frac{R^4\ \sin^2(\varepsilon)\ \sin^2(\theta)}{B_\odot \sigma_t \pi r_\odot^2 (1 + \cos^2(\theta + \varepsilon)) \sin^4(\theta + \varepsilon)} dI, \qquad (11)$$

which gives the electron count in closed form for small features. The only remaining geometry is (1) the solar elongation of the feature, $\varepsilon$; (2) the exit angle $\theta$; and (3) $R$, the Sun–observer distance. The quantity $dN_e/dI$ is plotted in Figure 7. (For consistency with earlier figures, we have plotted the out-of-sky-plane angle $\xi$ rather than the exit angle $\theta$ as the two angles are complements.) As in earlier plots, the location where each plot line intersects the TS is indicated. Along lines of sight, in the vicinity of the Thomson plateau, the inferred electron count scales as $z^2$ (simple geometric distance from the observer) because the feature's inferred surface density is nearly constant (Figure 8). Farther away, the curve transitions smoothly to $z^4$ dependence at large angles (large negative $\xi$) because $z \sim r$ at large distances and both perspective and illumination effects are important. At constant $r$, inferred densities roll over because the illumination is constant and $z$ has a maximum at 2 AU when $\xi = -90°$.

The left panel of Figure 7 shows how to calculate the mass (or, at least, electron count) in a feature with a known $\varepsilon$ and a given intensity—that is to say, a given total summed or integrated image pixel value on the image plane of the observing instrument. For example, an object observed from 1 AU at $\varepsilon = 20°$ (solid red line) at the TS would have to contain approximately $5 \times 10^{38}$ electrons to deliver one

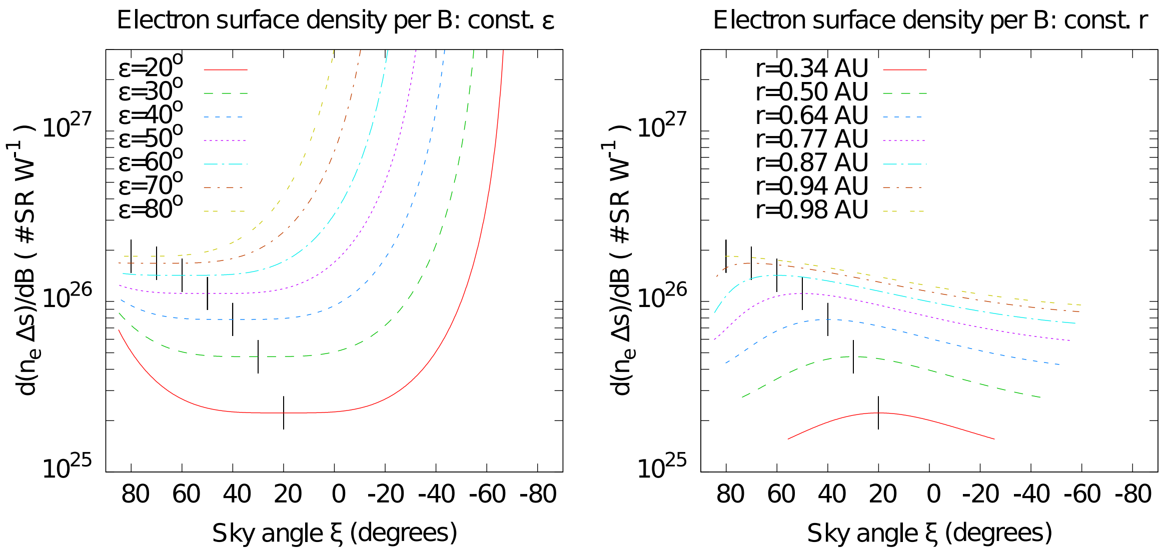


**Figure 8.** Plots of the density calculation coefficient $d(n_e ds)/dB$ show that inferred feature surface density is independent of solar exit angle for a wide range of angles, reflecting the flatness of the Thomson plateau (Equation (2)). Curves and features are the same as in Figure 7.

(A color version of this figure is available in the online journal.)

nW m$^{-2}$ (nanoWatt per square meter) of scattered sunlight to the instrument aperture. The Thomson plateau is visible in the left panel of Figure 7 as a flat but tilted region of each plotted line near the marked location of the TS. Within the plateau, the feature surface brightness remains approximately constant with $\xi$, and the $z^{-2}$ dependence of feature size is evident in the slope of each curve across the Thomson plateau, centered on the marked location of the TS. The TS is neither a local maximum nor minimum for this calculation, reflecting the fact that perspective (proximity) effects dominate the total mass calculation in this region. The right panel shows the same calculation, with fixed $r$ rather than fixed $\varepsilon$. The TS is marked and the curves coincide across the two panels at the TS. It should be clear from Figure 7 that the TS plays no particularly important role in the calculation of mass from small, local features.

The left panel of Figure 8 shows how to calculate the electron surface density (the electron density integrated along the LOS) in a feature with a known solar elongation and a given surface brightness (i.e., a given average pixel value inside the feature in the image plane). For example, an object observed from 1 AU at $\varepsilon = 20°$ (solid red line) at the TS would have to contain approximately $2 \times 10^{16}$ electrons m$^{-2}$ of cross-section (from the point of view of the observer), to deliver 1 nW m$^{-2}$ SR$^{-1}$ of light ($5 \times 10^{-17} B_\odot$) to the instrument aperture. The Thomson plateau is clearly visible near the marked TS because perspective effects do not change the surface brightness of observed features. The inferred surface density of electrons is independent of solar exit angle for a broad range of exit angles, reflecting the flatness of the $G$ function plotted in Figure 2.

The right panel of Figure 8 shows the same calculation, with fixed $r$ rather than fixed $\varepsilon$. The TS is marked and the curves coincide across the two panels at the TS. It is important to note that the TS is a local maximum in each curve in that panel, reflecting the inefficiency of Thomson scattering near the TS. Objects at the TS must have higher electron surface density to produce a given radiance than objects far from the TS at the same radius.

## 3. OBSERVATIONAL EVIDENCE

White light coronal and solar wind observations have until recently been made exclusively by coronagraphs. The small angular range covered by coronagraphs and the single observer perspective have limited the effects of the extent of the region of major scattering contribution, which do not involve significant distances until we are at large angles from the Sun. Kinematic parameters such as speed and acceleration were made with the understanding that they were lower limits due to projection effects into the sky plane (e.g., Howard et al. 2008b). Recently, heliospheric imager observations have expanded our FOV to much larger angles. Analytical attempts to locate features in 3D space have been fraught with difficulties. The problems arise in part because objects in the heliosphere are visible from an extremely broad range of distances along the LOS.

Section 2 presents the argument in theoretical terms that the TS is not important when identifying and measuring features observed in the heliosphere. One prediction that arises from this theory is that objects located far from the TS should be nearly as readily seen as those near the TS. Observations of large-scale transient phenomena have been recorded demonstrating that this is indeed the case. In this section, we review some examples of features observed very far from the TS. We focus on two phenomena: corotating interaction regions (CIRs) and far-side CMEs.

### 3.1. Corotating Interaction Regions

A CIR (Smith & Wolfe 1976) is a compression region brought about by the interaction between a column of fast-flowing solar wind and the surrounding slow wind (Pizzo 1978, 1980, 1982). The interaction occurs because the fast wind stream co-rotates with the Sun, and so CIRs are more commonplace at low solar latitudes. In a time-stationary reference frame, their simplest description is that resembling the so-called Parker spiral.

Although they are not observed by coronagraphs, CIRs have been identified and tracked with heliospheric imagers. Sheeley et al. (2008) discussed observations of the inner component

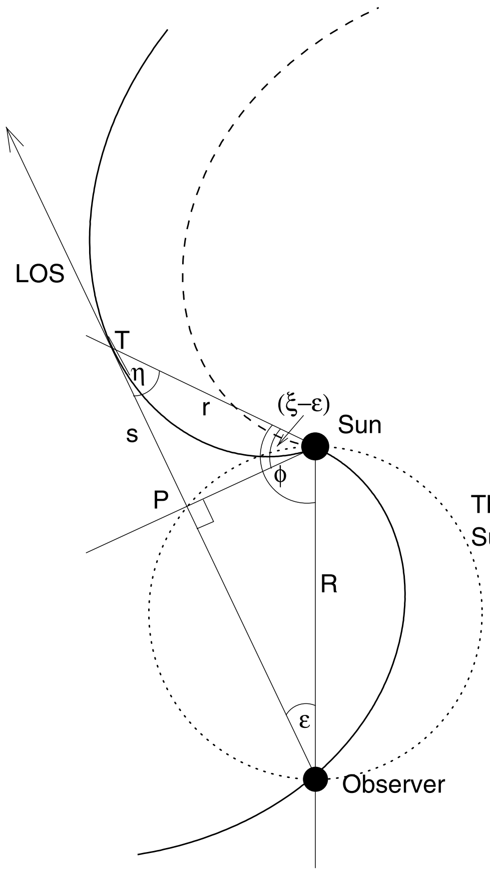


**Figure 9.** Geometry of a CIR at various times during its rotation compared with the Thomson surface (the dashed circle). The CIR (heavy spiral arm) is shown at three locations: at the time of impact with the observer; 10 days prior to impact; and 12 days prior to impact (dashed). The location of the CIR is measured at the point where the line of sight (LOS) from the observer crosses the CIR at a tangent, as shown. This LOS also crosses the Thomson surface at P. The difference between the observed point and that along the TS is therefore the angle between the Sun-tangent vector and the vector passing through P (we denote this angle $(\xi - \varepsilon)$). The remaining terms are similar to Tappin & Howard (2009a), but renamed for consistency with Section 2.

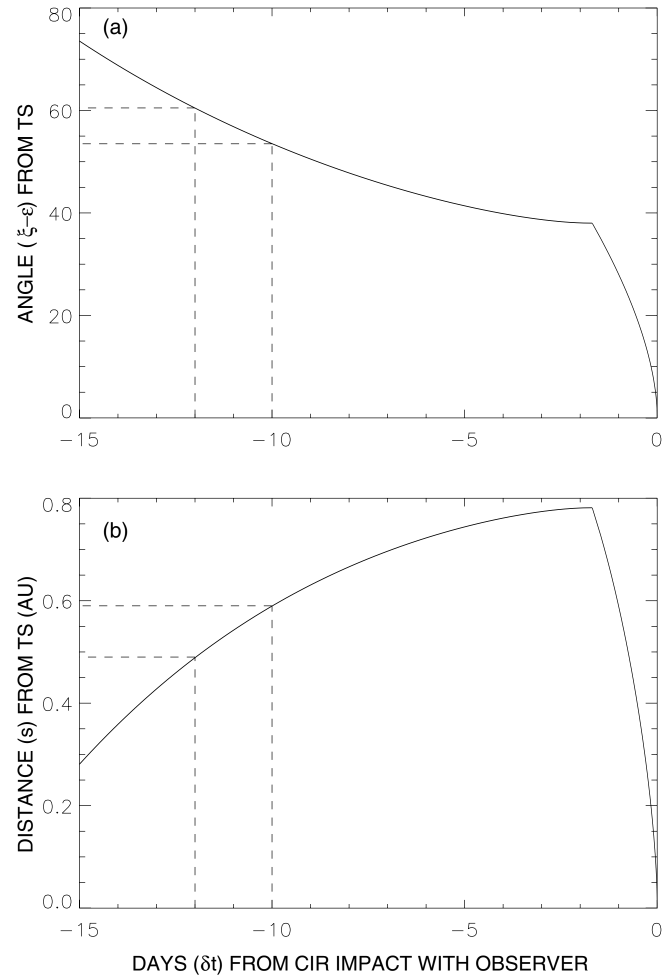


**Figure 10.** (a) The angular separation $(\xi - \varepsilon)$ between the Thomson surface and the measured point along the tangent of a CIR at a solar wind speed of 400 km s$^{-1}$, plotted against time before impact with the observer ($\delta t$ in Tappin & Howard 2009a). (b) Distance $s$ vs. the same time period ($s = \sin(\xi - \varepsilon)$). The dashed lines represent 10 days prior to impact with the observer, where CIRs are known to be observed by heliospheric imagers; and 12 days prior, where CIRs are probably observed. These correspond to $(\xi - \varepsilon)$ values of 53$^\circ\!.$5 and 60$^\circ\!.$5 and $s$ values of 0.59 AU and 0.49 AU, respectively. The reader will note that the nature of both curves suddenly change at −1.69 days before impact. At this time the leading edge of the CIR reaches 90° elongation. Beyond this time $(\xi - \varepsilon)$ is equivalent to $\phi$.

of the spiral observed by *STEREO-B*, Rouillard et al. (2008) measured the outer component observed by *STEREO-A*, and Wood et al. (2010) derived a 3D model from both *STEREO-A* and *STEREO-B* measurements of morphology. Tappin & Howard (2009a) discuss the observation of both inner and outer components and also CIR observation by SMEI. Rouillard et al. (2008) and Tappin & Howard (2009a) demonstrate that the CIR can be observed clearly at least 10 days prior to its arrival at the Earth, and the results of the latter suggest it may be tracked back as far as 12 days.

CIRs are visible for as long as 10–12 days to the east of the Sun before impact with Earth, implying a rotational sweep of 130°–155° due to the 28 day period solar rotation. In order to identify the relationship between the observed component of the CIR and TS, consider the geometry shown in Figure 9. The location of the CIR is shown for three separate times, and the observing geometry is constructed for the period 10 days prior to impact with the observer. The measured location of the CIR (i.e., the corresponding feature) is the elongation angle $\varepsilon$ where the LOS crosses the CIR at a tangent (at point T in Figure 9). The LOS also crosses the TS (at P), and the angle between P and the tangent point is labeled $(\xi - \varepsilon)$. From the geometry in Figure 9 it is clear that $(\xi - \varepsilon) = \pi/2 - \chi$. This is the angular separation between the TS and the measured point for a CIR.

Figure 10(a) shows a plot of $(\xi - \varepsilon)$ versus $\delta t$ for a CIR with a solar wind speed of 400 km s$^{-1}$ (following the theory of Tappin & Howard 2009a). The curve shows an increasing angular separation from the TS as we move further from the time of impact. Ten days prior to impact the separation is $\sim$53$^\circ\!.$5 and 12 days prior it is $\sim$60$^\circ\!.$5. Figure 10(b) shows the variation of physical distance $d = r \sin(\xi - \varepsilon)$ for the same CIR across the same time. The distances of the CIR front 10 and 12 days prior to impact are shown as 0.59 and 0.49 AU, respectively. The greatest distance occurs when the leading edge of the CIR appears at an elongation of 90°: This is also the elongation beyond which the greatest scattering contribution lies in the immediate vicinity of the observer. The distance from the TS of this point is 0.78 AU. CIRs are therefore visible over 50° (and probably >60°) from the TS, and also at distances approaching 0.8 AU away.

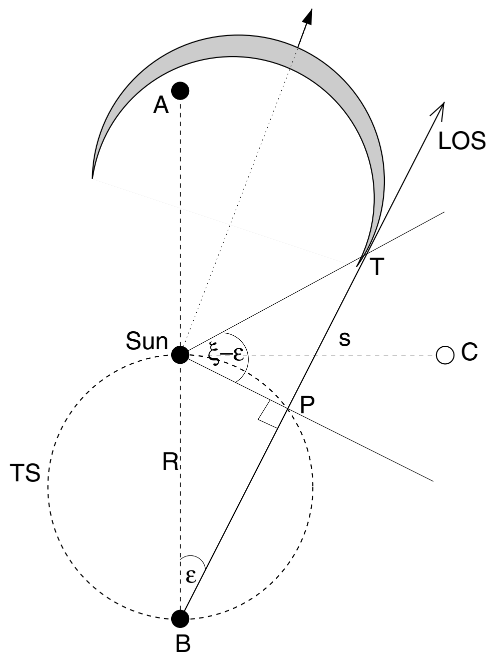


**Figure 11.** Diagram of a backsided CME heading toward one observer A that is located on the opposite side of the Sun to another observer B. A third observer C is also located perpendicular to the AB line. The example CME illustrated here has a width of 90° and oriented so it impacts A but misses both B and C. The TS is indicated and angles are labeled so as to correspond with Figure 9. This situation is analogous to the configuration of the *STEREO* spacecraft at their most recent orbit phase with Earth perpendicular to them at point C.

### *3.2. Coronal Mass Ejections*

While backsided CMEs (CMEs traveling away from the observer) have been observed since CMEs were discovered (e.g., DeMastus et al. 1973; Gosling et al. 1974, 1976; Munro et al. 1979) this was not regarded as unusual, as the physical distance between the plane of the sky and the CME in the coronagraph FOV is at most times relatively small. Heliospheric imagers cover a larger part of the sky and so their fields of view cover much larger distances. To our knowledge, no backsided CME was ever confirmed with SMEI (probably because SMEI performed best at elongations beyond 45°), but they have recently appeared in *STEREO*/HI data. In the most recent phase of the *STEREO* mission, the two spacecraft are at opposition, i.e., they are currently on opposite sides of the Sun at distances near 2 AU from each other. Therefore during this phase any CME headed toward one *STEREO* spacecraft must be backsided relative to the other. In situ assets on board *STEREO* indicate the arrival of the CME there, which sets a limit for one of the CME boundaries. We also have a third observer at Earth, which enables a limit on the other boundary. Here we discuss a number of cases involving backsided CMEs that have been observed by the heliospheric imagers.

Consider the situation illustrated in Figure 11, where an example of a backsided CME relative to observer B moves toward a second observer A. The angle $(\xi - \varepsilon)$ shows the angle between the TS and the leading edge measurement. This is for a single example case of a CME that is 90° wide that passes A but misses both B on the opposite side of the Sun and a third observer (C) perpendicular to the A–B line, as in the *STEREO* spacecraft at opposition with Earth located at C. The distance $s$ from the TS to the tangent point $T$ crossing the CME (the feature) is related to the elongation $\varepsilon$ and TS angle $(\xi - \varepsilon)$ by

$$s = R \sin \varepsilon \tan(\xi - \varepsilon), \qquad (12)$$

where $R$ is the distance from the Sun to observer B.

One event, observed by SMEI and reported by Howard et al. (2007), was located by solar surface associations just behind the east solar limb. This event, observed in 2004 February, was tracked out to around 35° elongation, or ∼0.6 AU from the Sun. These results were cited by Howard & Tappin (2009) as not supporting the TS localization view. *STEREO* results of Lugaz et al. (2011) and the SMEI team (S. J. Tappin 2011, private communication) show a number of recent events that have been located in a single quadrant of the heliosphere using auxiliary data sets, but observed by the heliospheric imagers of the *STEREO* spacecraft in the opposite quadrant. In other words, backsided CMEs have been observed by the HIs. Table 1 shows a list of 10 of these events. Note that seven events were tracked beyond 30° elongation and one beyond 40°.

## 4. DISCUSSION AND CONCLUSIONS

We have demonstrated that heliospheric imagers are sensitive to features at a wide variety of exit angles from the Sun, and that heliospheric radiance photometry is insensitive to LOS effects over a surprisingly wide range of angles, which we call the "Thomson plateau." On the Thomson plateau, a fortuitous cancellation renders instrument sensitivity to electron density independent of an object's location along the LOS to a very good approximation. We have shown that, although the TS is a useful geometric tool for understanding broad-field perspective, the TS itself is not particularly important for photometric interpretation of unpolarized heliospheric images. On the contrary, its primary importance is that it marks the center of the Thomson plateau, where instrument pixel response (measured in radiance per unit LOS-integrated electron density) is essentially independent of exit angle effects.

Further, the TS does not define a locus of particularly high sensitivity for detection of heliospheric features with unpolarized Thomson scattered light. In fact, because of the physics of Thomson scattering, the TS represents a *minimum* in instrument pixel response, if the feature's distance from the Sun be held fixed and the elongation be allowed to vary. While the numeric electron density along a given LOS is typically greatest near the TS, the effect does not strongly filter detection of interesting dense features such as CMEs and CIRs, and in fact we have demonstrated imaging of such features more than 90° from the center of the Thomson plateau. There are two main reasons for this lack of importance: (1) individual objects of interest are typically dense enough to stand out from fluctuations in the density of the background solar wind, so that the weak maximum in average density near the TS does not overwhelm other features on the same LOS; and (2) heliospheric imagers do not suffer from the strong radial gradient in background brightness that is observed with coronagraphs, so that perspective effects that reduce the elongation of a particular feature do not necessarily hide that feature behind a bright noise field.

Finally, aside from breaking the front/back symmetry that is apparent in coronagraphs, the TS does not bear any special geometric relationship to either the problem of heliospheric object detection, or the problem of feature mass measurement. Both the detection and the mass measurement problems are dominated by perspective effects, in part because of the flatness of the Thomson plateau and in part because those effects

**Table 1**
Properties of Backsided CMEs that have been Observed by the *STEREO*/HIs

| No. | Date and Time of First Appearance | *STEREO* Separation | Heading Toward | Observed by | Maximum $\varepsilon$ | Source |
|---|---|---|---|---|---|---|
| 1 | 2009 Jul 10 ~10UT | 104°.1 | B(I) | HI-2A | 27° | Lugaz et al. (2011) |
| 2 | 2009 Jul 26 11:35 | 106°.5 | B(I) | HI-2A | 38° | Lugaz et al. (2011) |
| 3 | 2009 Sep 26 17:45 | 106°.5 | B(I) | HI-1A | 15° | Lugaz et al. (2011) |
| 4 | 2009 Nov 8 05:25 | 125°.8 | A(I) | HI-2B | 30° | Lugaz et al. (2011) |
| 5 | 2009 Nov 5 08:05 | 127°.9 | B(I) | HI-2A | 24° | Lugaz et al. (2011) |
| 6 | 2009 Nov 22 ~14UT | 127°.9 | B(I) | HI-2A | 39° | Lugaz et al. (2011) |
| 7 | 2009 Dec 4 06:50 | 129°.5 | A(I) | HI-2B | 32° | Lugaz et al. (2011) |
| 8 | 2010 Apr 19 14:25 | 139°.6 | A(I) | HI-2B | 37° | Lugaz et al. (2011) |
| 9 | 2011 Nov 9 13:36 | 151°.4 | BE | HI-2A | 42° | S. J. Tappin |
| 10 | 2011 Nov 26 07:00 | 148°.3 | EA | HI-2B | 36° | S. J. Tappin |

**Notes.** In the fourth column the *STEREO* spacecraft is indicated (A or B) and an (I) label indicates that it impacted that spacecraft (i.e., the CME was measured by the in situ instruments on board). BE and EA indicate that the CME was in the quadrant between Earth and *STEREO-B* (or *-A*). Where S. J. Tappin is named, this refers to a private communication (2011).

overwhelm the illumination function for features passing close by the observer.

The Thomson plateau represents a wide locus in which inferred electron density is independent of solar exit angle, and in which, therefore, electron surface density of features may be measured precisely even without precise location of those features in three dimensions. Because the plateau has sharp edges and steep sides, it may be possible (as described by Vourlidas & Howard 2006) to estimate the trajectory of a CME near the sky plane by matching its extracted brightness profile (e.g., DeForest et al. 2011) to a particular exit angle brightness deficit curve. But the flatness of the plateau limits the usefulness of that technique for precisely the CMEs that are of most interest (those that are headed in the general direction of the observer) because of the bias of the TS toward the observer at large elongation angles. That bias implies that there is no brightness deficit, for a broad range of elongations, in features that are headed toward the observer. For those CMEs, other techniques are needed to localize the feature, such as polarized imaging or geometric analysis (e.g., Lugaz et al. 2009; Tappin & Howard 2009b).

Our results highlight the importance of separating measurements of radiance (which is approximately independent of perspective effects, and which is approximated by the area *averaged* pixel value in a heliospheric image) from intensity (which depends strongly on perspective effects, and is approximated by the area *summed* pixel value in a heliospheric image), and in the single pixel case differs from radiance by a factor of the area scale of a pixel. The former is proportional to LOS-integrated surface density and is approximately constant on the Thomson plateau; the latter is proportional to total feature mass and decreases monotonically as observer–object distance increases.

To conclude, we have used elementary Thomson scattering theory to demonstrate proper technique for forward-modeling observed feature intensity and brightness in the heliosphere, and for calculating feature mass and instrument sensitivity in simple cases. Further, we have addressed three pervasive misconceptions that have developed surrounding the TS. First, the TS does not represent a sharp maximum of radiance per electron in the heliosphere along a given LOS: The maximum is spread across a broad range of angles, forming instead a "Thomson plateau" over which radiance at a heliospheric imager focal plane is nearly independent of position along the LOS. Second, mass inference from heliospheric images is not as strongly affected by the geometry of the TS or Thomson plateau as by other factors. Third, sensitivity of unpolarized heliospheric imagers is not strongly affected by geometry relative to the TS, and in fact CMEs have been observed very far from the TS with current heliospheric imagers. The latter two considerations are dominated instead by perspective effects in physically interesting cases (propagation toward the observer). The TS does become more important when polarized light is considered; we will treat polarized light in Paper II of this series.

The authors thank S. J. Tappin, N. Lugaz, and A. Vourlidas for providing some of the observational results and for their comments. Additional thanks to S. J. Tappin for theoretical discussions for this and in papers leading to the present report. Support for this work is provided in part by the NSF/SHINE Competition, Award 0849916 and the NASA Heliophysics program through grant NNX10AC05G.

## REFERENCES

Billings, D. E. 1966, A Guide to the Solar Corona (San Diego, CA: Academic)
Brueckner, G. E., Howard, R. A., Koomen, M. J., et al. 1995, Sol. Phys., 162, 357
DeForest, C. E., Howard, T. A., & Tappin, S. J. 2011, ApJ, 738, 103
DeMastus, H. L., Wagner, W. J., & Robinson, R. D. 1973, Sol. Phys., 100, 449
Eyles, C. J., Harrison, R. A., Davis, C. J., et al. 2009, Sol. Phys., 254, 387
Eyles, C. J., Simnett, G. M., Cooke, M. P., et al. 2003, Sol. Phys., 217, 319
Gosling, J. T., Hildner, E., MacQueen, R. M., et al. 1974, J. Geophys. Res., 79, 4581
Gosling, J. T., Hildner, E., MacQueen, R. M., et al. 1976, Sol. Phys., 48, 389
Guhathakurta, M., Fisher, R. R., Holzer, T. E., & Sime, D. G. 1993, BAAS, 25, 1213
Hecht, E., & Zajac, A. 1979, Optics (4th ed.; Menlo Park, CA: Addison-Wesley)
Howard, R. A., Moses, J. D., Vourlidas, A., et al. 2008a, Space Sci. Rev., 136, 67
Howard, R. A., Vourlidas, A., Plunkett, S. P., et al. 2010, AGU 2010, Fall Meet. Suppl. Abstract SH11B-1627
Howard, T. A., & DeForest, C. E. 2012, ApJ, 746, 64
Howard, T. A., Fry, C. D., Johnston, J. C., & Webb, D. F. 2007, ApJ, 667, 610
Howard, T. A., Nandy, D., & Koepke, A. C. 2008b, J. Geophys. Res., 113, A01104
Howard, T. A., & Tappin, S. J. 2009, Space Sci. Rev., 147, 31
Jackson, J. D. 1962, Classical Electrodynamics (New York: Wiley)
Koomen, M. J., Detwiler, C. R., Brueckner, G. E., Cooper, H. W., & Tousey, R. 1975, Appl. Opt., 14, 743
Lugaz, N., Kintner, P., Jian, L. K., et al. 2011, EOS Trans. AGU 92, Fall Meet. Suppl. Abstract SH23C-1972
Lugaz, N., Vourlidas, A., Roussev, I. I., & Morgan, H. 2009, Sol. Phys., 256, 269

Lyot, M. B. 1939, MNRAS, 99, 578
MacQueen, R. M., Csoeke-Poeckh, A., Hildner, E., et al. 1980, Sol. Phys., 65, 91
MacQueen, R. M., Eddy, J. A., Gosling, J. T., et al. 1974, ApJ, 87, L85
Michels, D. J., Howard, R. A., Koomen, M. J., & Sheeley, N. R., Jr. 1980, in Radio Physics of the Sun, ed. M. R. Kundu & T. E. Gergely (Hingham, MA: Reidel), 439
Minnaert, M. 1930, Z. Astrophys., 1, 209
Munro, R. H., Gosling, J. T., Hildner, E., et al. 1979, Sol. Phys., 61, 201
Pizzo, V. 1978, J. Geophys. Res., 83, 5563
Pizzo, V. 1980, J. Geophys. Res., 85, 727
Pizzo, V. 1982, J. Geophys. Res., 87, 4374
Rouillard, A. P., Davies, J. A., Forsyth, R. J., Hapgood, M., & Perry, C. H. 2008, Geophys. Res. Lett., 35, L10110
Schuster, A. 1879, MNRAS, 40, 35
Sheeley, N. R., Jr., Herbst, A. D., Palatchi, C. A., et al. 2008, ApJ, 675, 853
Smith, E. J., & Wolfe, J. H. 1976, Geophys. Res. Lett., 3, 137
Tappin, S. J., & Howard, T. A. 2009a, ApJ, 702, 862
Tappin, S. J., & Howard, T. A. 2009b, Space Sci. Rev., 147, 55
Tousey, R. 1973, Space Research 13 (Berlin: Akademie-Verlag), 713
van de Hulst, H. C. 1950, Bull. Astron. Inst. Neth., 11, 135
van Houten, C. J. 1950, Bull. Astron. Inst. Neth., 11, 160
Vaseghi, S. V. 2006, Advanced Digital Signal Processing and Noise Reduction (Chichester: Wiley)
Vourlidas, A., & Howard, R. A. 2006, ApJ, 642, 1216
Wood, B. E., Howard, R. A., Thernisien, A., & Socker, D. G. 2010, ApJ, 708, L89